Computer Assisted Methods in Engineering and Science, **21**: 151–167, 2014.

Analysis of fluid-structure interaction of a torus subjected to wind loads

Agnieszka Padewska, Piotr Szczepaniak, Andrzej Wawrzynek
Department of Theory of Building Structures
Faculty of Civil Engineering
Silesian University of Technology
Akademicka 5, 44-100 Gliwice, Poland
e-mail: agnieszka.padewska@polsl.pl

In the paper the aerodynamic forces acting on a part of a water slide or other object with curved, tubular shape, depending on the section of a torus and value of the wind velocity, were obtained. This was done by means of *finite element method* (FEM) and *finite volume method* (FVM) computer simulations, using modules: *computational fluid dynamics* (CFD) and *fluid-structure interaction* (FSI) and taking into account the Eurocode EN 1991-1-4.

Keywords: fluid-structure interaction, water slide, wind action, CFD, FSI, FEM, FVM.

1. Introduction

One of the significant natural phenomena that should be taken into account in the design of the structure is wind. Pressure and suction forces depend on many factors, such as: speed, direction and density of flowing air masses, shape, dimensions and stiffness of the building and its location (its surrounding area).

This work is a presentation of subsequent steps of complicated creating of numerical models and determining forces acting on: 1) the cylinder perpendicular to the gas flow direction and 2) the object in the shape of circularly bent pipe. Just mentioned steps consist of:

- creating a geometry of the calculation area;
- proper setting of gas characteristics, object characteristics and boundary conditions;
- determining an appropriate turbulence model;
- determining appropriate methods of calculating gas flow;
- creating appropriate FEM and FVM meshes of the area around the wall of the object in order to accurately reflect the changes in the velocity gradient in the boundary layer and to transfer a pressure force from CFD to the mechanical application faces;
- determining drag coefficient for a cylinder perpendicular to the gas flow;
- transferring the pressure from the near-wall region to the structural analysis;
- determining wind force acting on an object in the shape of circularly bent pipe.

Particularly for new and large constructions, like water slides, experimental data from wind tunnel tests are not available. Fluid-structure interactions are a crucial element to be considered in the design of many engineering systems. It is the interaction of a structure with an internal or surrounding fluid flow. Since in the cases, which are described in this paper, deformations and displacements are ignored, one-way FSI is used for its lower computational requirements. It enables, e.g., calculations of the wind actions on each part of the water slide.

Results obtained from numerical analysis of wind flow around a cylinder perpendicular to wind velocity direction are compared to the force coefficients given in the Eurocode EN 1991-1-4. Due to the fact that the Eurocode [5] does not include practical design regulations of objects in the unusual shape of a bent pipe the aerodynamic forces of that object were briefly analyzed. The results of numerical analysis: FEM and FVM (with application of modules: CFD and FSI) are presented, too.

2. Numerical models of wind flow around a cylinder – comparison with european standards and experimental tests

The fluid domain is defined as a rectangular solid with the cylindrical cut inside. Figure 1 shows the entire exemplary fluid domain with dimensions and boundary conditions. The diameter of the cylinder is $b = 1.0$ m. The computational model dimensions are chosen such that the inlet, outlet and far-field boundaries are far enough from cylinder's surface to avoid any boundary effects, according to [3, 7, 9]. Air enters the flow domain perpendicular to the wall with uniform velocity. Symmetry, which is essentially a wall with slip condition, is chosen for the top and bottom boundary to reduce computational time. Since the future works will include simulations of flow past a yawed and inclined circular cylinder, the current domain is three-dimensional. In the through-thickness direction the domain is modeled with one-element and appropriate symmetry boundary conditions on the faces in this direction are imposed to recover 2D behavior and to constrain the out-of-plane flow. A non-slip wall boundary condition is applied at the cylindrical surface of a water slide with equivalent surface roughness $k_e = 0.15$ mm which corresponds to the surface of a fiberglass laminate. Figure 5 and experimental tests show that force coefficient c_f highly depends on surface roughness. All velocity w components are set equal to 0. At the downwind boundary the pressure outlet is used with the relative pressure specified at 0 Pa.

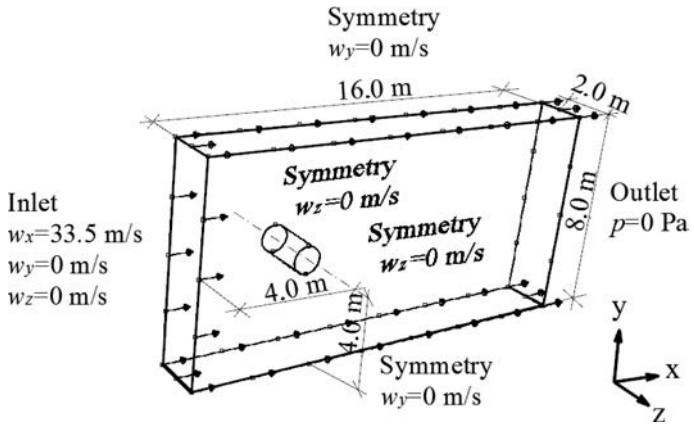

Fig. 1. Dimensions and boundary conditions for the exemplary model of air flow.

The fluid is modeled as an incompressible Newtonian fluid. The fluid density is chosen to be $\rho = 1.25$ kg/m^3 and the viscosity is $\mu = 1.875 \cdot 10^{-5}$ Pa·s, according to EN 1991-1-4.

According to [3], there are two kinds of solvers available in FLUENT: *pressure-based* and *density-based* ones. In this paper the *pressure-based* solver is chosen because it is applicable for a wide range of flow regimes. These solvers are used to take momentum and pressure (or pressure correction)

as the primary variables. The algorithm for the solution of the Navier-Stokes equations relies on the implicit segregated pressure-velocity formulation such as *SIMPLE* (semi-implicit method for pressure-linked equations) scheme, according to [9] and [16]. It is unclear which of the schemes is the best for general purpose computation, but the segregated solution method is best suited, e.g., for incompressible flows. *Standard* interpolation scheme for calculating cell-face pressures is acceptable for most cases and it is not as computationally expensive as the other schemes. It is used to reduce accuracy for flows exhibiting large surface-normal pressure gradients near boundaries. The *second-order upwind* interpolation scheme is chosen to use larger stencils for second-order accuracy which is essential when flow is not aligned with grid. Finally, the *transient* option is selected to enable the transient solver.

According to [9], time step must be small enough to resolve time-dependent features. However, the round-off error (the difference between the machine accuracy of a computer and the true value of a variable) increases with step size while the discretization error decreases. Acceptably reasonable compromise can be determined from:

$$\Delta t < \frac{b}{n \cdot Sr \cdot w}. \tag{1}$$

The Strouhal number for flow past cylinder is roughly $Sr = 0.2$. In order to capture the shedding correctly, in one shedding cycle should be at least $n = 20$ time steps. In this paper time step size equal to 0.002 s is applied. The 10-fold reduction of Δt resulted in no change in the aerodynamic forces values.

As the flow begins its transition to turbulence, chaotic oscillations appear and it is no longer possible to assume that the flow is steady in time. Therefore, it is necessary to solve the problem in the time domain and the used mesh must be fine enough to resolve the size of the smallest eddies in the flow. An increase in Reynolds number results in the appearance of small eddies and such short timescales of the oscillations that it is computationally impossible to solve the Navier-Stokes equations. In this flow regime, e.g., the *Reynolds-averaged Navier-Stokes* (*RANS*) formulation can be used which is based on the observation that the flow field over time contains small, local oscillations that can be treated in a time-averaged sense. As a consequence, additional unknowns are added to the system of equations and approximations for the flow field at the walls are introduced.

ANSYS Fluent offers several different formulations for solving turbulent flow problems. Models computing fluctuation quantities like: the *detached eddy simulation* (*DES*), *large eddy simulation* (*LES*) or *direct numerical* simulation (*DNS*) are used to resolve the shorter length scales than models solving *RANS* equations. Hence they have the ability to provide better results. However, these models and simulations, especially the *DNS*, are often computationally expensive in comparison to the conventional one- or two-equation models (*RANS*). When using *RANS* models reliable results are obtained. For example, according to [6], application of the so called *shear-stress transport (SST) k-ω* model yields very similar results to experimental data for flow over a NACA 0012 airfoil.

According to [3] and [18], the k-ω model is useful in many cases where the k-ε model is not accurate, such as internal flows, flows that exhibit strong curvature, separated flows and jets. The first transported variable is turbulent kinetic energy k. The second transported variable is either the turbulent dissipation ε, or the specific dissipation ω. These are the variables that determine the scale of the turbulence, whereas the first variable k determines the energy in the turbulence. They are the rate at which turbulence kinetic energy is converted into thermal internal energy. Sometimes the specific turbulence dissipation ω is also referred to as the mean frequency of the turbulence. However, the disadvantage of the standard k-ω model is that it is dependent on the free-stream value of ω. Both the k-ε and k-ω models were combined by Menter [10, 11] and [12] in order to improve them. Consequently, the eddy-viscosity *SST* k-ω model was created which includes two main novelties:

- to blend these models together (k-ω in the near-wall region and k-ε model in the far-field) the standard k-ε model has been transformed into equations based on k and ω which lead to the introduction of a cross-diffusion term,
- a limitation of the shear stress in adverse pressure gradient regions is introduced.

These features make the *SST* k-ω model more accurate and reliable for a wider class of flows (for example, adverse pressure gradient flows, airfoils, transonic shock waves, flow separation) than the standard k-ω model. The *SST* k-ω model does produce a bit too large turbulence levels in regions with large normal strain like stagnation regions and regions with strong acceleration. This tendency is much less pronounced than with a normal k-ε model though.

The *SST* k-ω model has a similar form of the transport equations to the standard k-ω model (see, e.g., [3]):

$$\frac{\partial}{\partial t}(\rho k) + \frac{\partial}{\partial x_i}(\rho k u_i) = \frac{\partial}{\partial x_j}\left(\Gamma_k \frac{\partial k}{\partial x_j}\right) + \widetilde{G}_k - Y_k + S_k \tag{2}$$

and

$$\frac{\partial}{\partial t}(\rho \omega) + \frac{\partial}{\partial x_j}(\rho \omega u_j) = \frac{\partial}{\partial x_j}\left(\Gamma_\omega \frac{\partial \omega}{\partial x_j}\right) + G_\omega - Y_\omega + D_\omega + S_\omega. \tag{3}$$

Only one constant $\sigma_{k,1}$ and the expression for turbulent eddy viscosity μ_t are different. In these equations u_i is the velocity decomposed into the mean (ensemble-averaged or time-averaged) and fluctuating components. $\widetilde{G}_k$ represents the generation of turbulence kinetic energy due to mean velocity gradients. G_ω represents the generation of ω. Y_k and Y_ω represent the dissipation of k and ω due to turbulence. Γ_k and Γ_ω represent the effective diffusivity of k and ω, respectively. S_k and S_w are user-defined source terms.

Turbulence in the atmospheric boundary layer can be quantified by the turbulence intensity:

$$I \equiv \frac{u'}{U} \equiv \frac{\sqrt{1/3(\overline{u'u'} + \overline{v'v'} + \overline{w'w'})}}{\sqrt{U_x^2 + U_y^2 + U_z^2}}, \tag{4}$$

where u' is the root-mean-square of the turbulent velocity fluctuations and U is the mean velocity. It gives a general idea of the level of turbulence in the boundary layer, but is not enough to characterize and define the turbulent structures as it treats the three velocity fluctuations with equal weight.

The turbulence in the wind can also be characterized by the gust wind speed factor defined as:

$$I \equiv \frac{U_{gust}}{\overline{U}_{hourly}}. \tag{5}$$

It characterizes the peak wind speed in a given time interval over the mean hourly wind speed. It is a function of the turbulence intensity and it also depends on the duration of the gust: the larger the time interval, the smaller the gust factor is.

According to [5], the turbulence intensity I at height z is defined as the standard deviation of the turbulence divided by the mean wind velocity:

$$I = \frac{1}{\ln(z/0.05)} \quad \text{for terrain categories II.} \tag{6}$$

The turbulence kinetic energy k can be determined from its relation to the turbulence intensity I (see [3]):

$$k = \frac{3}{2}(wI)^2. \tag{7}$$

Then, the specific turbulence dissipation is defined by

$$\omega = \frac{\varepsilon}{k} = \frac{0.164k^{1.5}}{0.4\delta}. \tag{8}$$

Boundary layer thickness δ, according to [9], is given by

$$\delta = 5.0\sqrt{\frac{\nu x}{w}}, \tag{9}$$

where ν is kinematic viscosity, according to [5], and x is the distance downstream from the start of the boundary layer.

In the calculations presented here it is assumed that the turbulent kinetic energy and the specific dissipation rate are equal respectively to: $k = 60.8$ m^2/s^2 and $\omega = 930.2$ 1/s for the thickness of boundary layer $\delta = 3$ mm, height above ground $z = 10$ m and velocity $w = 33.5$ m/s. From wide range calculations it turns out that the drag coefficient c_x, which is used to quantify the drag or resistance of an object in a fluid environment, such as air, is almost insensitive to k and ω parameter values as much as the 10-fold reduction of these values causes increasing of the average value of the drag coefficient of just 1.1%. Drag coefficient is defined in the usual way:

$$c_x = \frac{1}{0.5\rho w^2 A_{ref}} \frac{\int_{t_1}^{t_2} P_x \mathrm{d}t}{t_2 - t_1} \; [-], \tag{10}$$

where P_x is the drag force which is by definition the force component in the direction of the flow velocity and $A_{ref} = b \cdot l$ is the reference area.

The integral time-average value of the drag coefficient using: 1) the standard k-ω and RNG k-ε turbulence models results with $c_x = 0.64$ and 2) the SST k-ω or *DES* models – $c_x = 0.59$. Figure 2 represents time-series of the drag coefficients at wind speed $w = 33.5$ m/s by using two of the previously mentioned exemplary turbulence models.

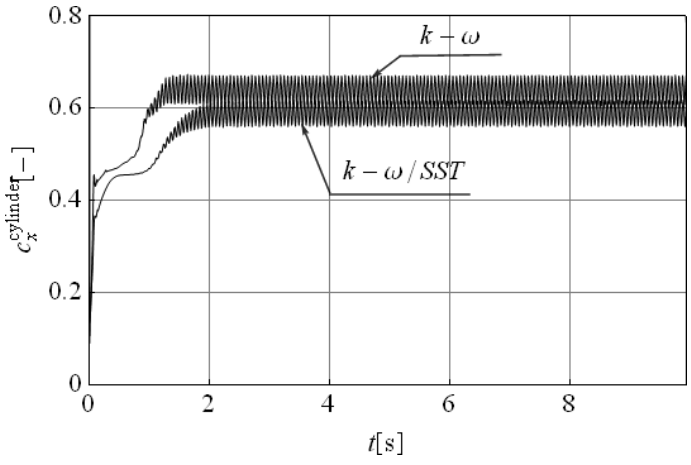

Fig. 2. Variation of the drag coefficient of the cylinder during first 10 s at the $w = 33.5$ m/s obtained from different turbulence models.

High quality numerical results for the wall boundary layer will only be obtained if the overall resolution of the boundary layer is sufficient but it requires only a mesh refinement in the wall-normal direction. Thirty-six layers of elements with a growth ratio of about 1.15 are established. The volume mesh is made up of 15 227 hexahedral cells of the regular repetition of an identifiable block belonging to the category of structured mesh. It is shown in Fig. 3.

a)

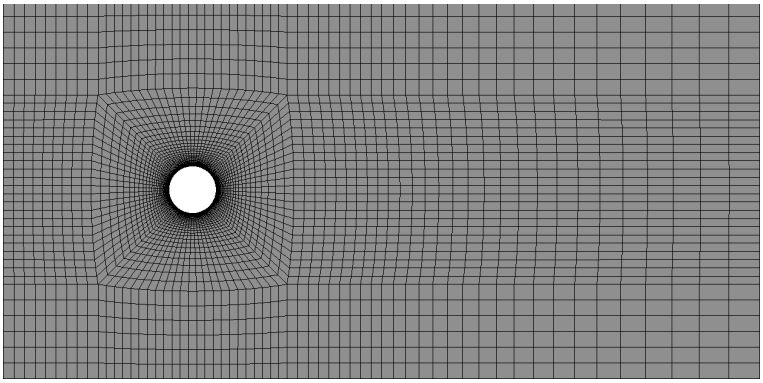

b)

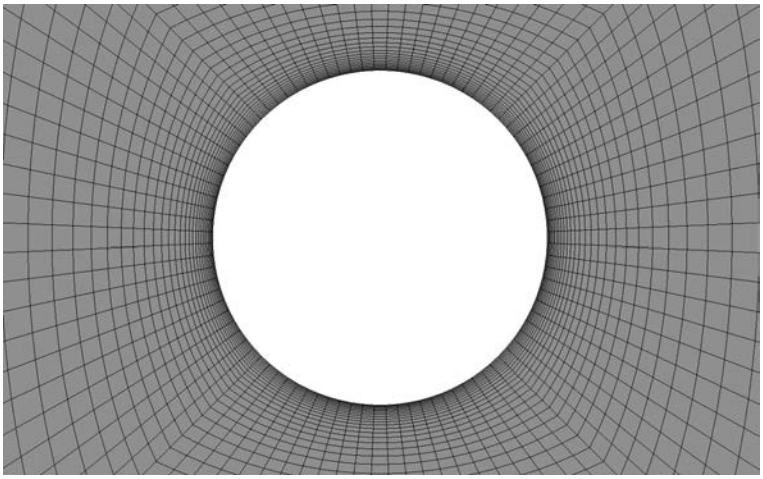

Fig. 3. FVM mesh of the model of wind flow around a cylinder: a) whole domain, b) near-wall region.

According to [3, 8, 16] and [18] the viscosity-affected region is made up of three zones (with their corresponding wall y^+ – non-dimensional wall distance from the wall to the first FVM mesh nodes or ratio between the turbulent and laminar influences in a cell), namely the:

- viscous sublayer ($y^+ < 5$),
- buffer layer or blending region ($5 < y^+ < 30$),
- fully turbulent or log-law region ($y^+ = 30$ to 60).

Further away from the wall the flow transitions occur in the free-stream region. It is possible to use a *RANS* model to compute the flow field in all four of these regimes. However, the thickness of the buffer layer is very small, so it can be beneficial to use an approximation in this region. Models have significantly lower computational requirements (a coarse mesh) when wall functions are used. The first computational node is placed in the fully turbulent inner region and suitable assumptions about how the near-wall velocity profile behaves are made, in order to obtain the wall shear stress.

A blending function depending on y^+ is used. The solutions for ω in the linear and the logarithmic near-wall region are (see [3] and [11])

$$\omega_{vis} = \frac{6\nu}{0.075y^2}, \tag{11}$$

$$\omega_{\log} = \frac{\sqrt[4]{\left(\frac{w}{y^+}\right)^4 + \left(\frac{w}{\log 9.8y^+}\right)^4}}{0.123y}, \tag{12}$$

where y is the cell centroid distance from the wall in the first FVM layer.

Table 1, depending on the speed of wind flow, shows: 1) the non-dimensional wall distance y^+, adopted according to [2, 3, 9, 16, 18] and 2) the values of the Reynolds number characterized by equation:

$$Re = \frac{b \cdot w}{\nu} = \frac{1 \cdot w}{15 \cdot 10^{-6}} \left[\frac{\mathrm{m} \cdot \mathrm{m/s}}{\mathrm{m^2/s}}\right], \tag{13}$$

where $b = 1$ m is a diameter of a cylinder and ν – kinematic viscosity, according to [5]. It is a measure of the ratio between inertial forces and viscous forces. Turbulent flows always occur at high Reynolds number. They are caused by the complex interaction between the viscous terms and the inertia terms in the momentum equation. The *Re* values applied in the calculations are in the critical and supercritical ranges of the turbulent flow.

Table 1. Summary of the *Re* values and FVM grid refinements.

w [m/s]	11 (strong breeze)	15 (high wind, moderate gale)	22 (strong gale)	33.5 (hurricane)
Re [–]	$7.3 \cdot 10^5$	10^6	$1.5 \cdot 10^6$	$2.2 \cdot 10^6$
y^+ [–] minimum	6	7	10	14
y^+ [–] coarse mesh	50	63	90	135
y^+ [–] fine mesh	6	7	40	50

The estimated first FVM element's height equals:

$$h = 2y = \frac{2\sqrt{74}}{Re^{13/14}} b y^+ = 3.0 \text{ mm} \tag{14}$$

for all cases from the Table 1 using a coarse mesh.

Cylindrical models which are perpendicular to the flow direction of the wind are analyzed. Computed variations of the time-average drag coefficient c_x for different y^+ values and for different wind velocity values w are shown in Fig. 4. The maximum values of the c_x coefficients for models with a coarse mesh are comparable (lower by about 5%) to the force coefficients values given in the European code [5] (see Figs. 4 and 5). Very similar results, differing by no more than 2 % of 2.5 D model (spatial model with one-element in the through-thickness direction) were achieved for the entirely spatial model.

In more accurate approach the obtained values of drag coefficient should be independent of the grid as long as we keep in mind that the cell centroid distance from the wall y should be greater than the equivalent surface roughness. The minimal values of y^+ are shown in Table 1 (assuming that the value of y is slightly greater than k_e). It also includes the maximum values of y^+ (a fine mesh) for which the drag coefficients remain almost unchanged, it means that difference between solutions for different small y^+ is less than 5% (according to Fig. 4 – part of curves for y^+ from the range 0–50). According to [3, 10–12], the wall boundary conditions for the k Eq. (2) in the k-ω models are treated in the same way as the k equation is treated when enhanced wall treatments are used with the k-ε models. This means that for all boundary conditions a low-Reynolds number formulation (in which the location of the near-wall grid node of a fine mesh is virtually moved down through the viscous sub-layer) is switched automatically to a wall function treatment, when a coarse mesh ($y^+ > 30$) is used (and the near-wall grid point is treated as being outside the edge

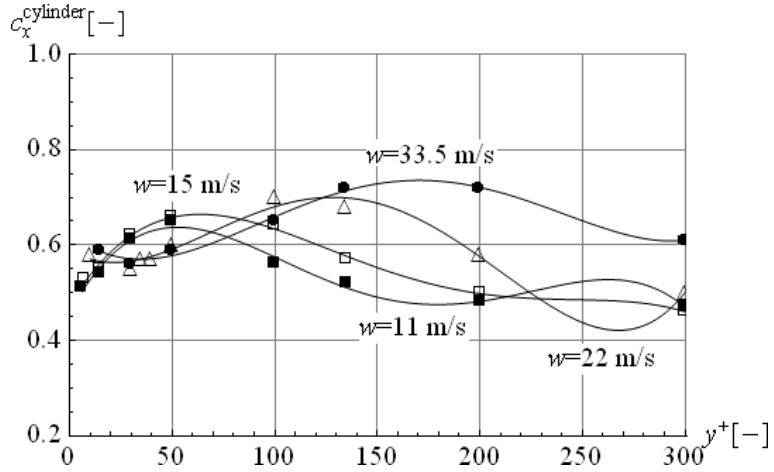

Fig. 4. Force coefficients according to grid refinements.

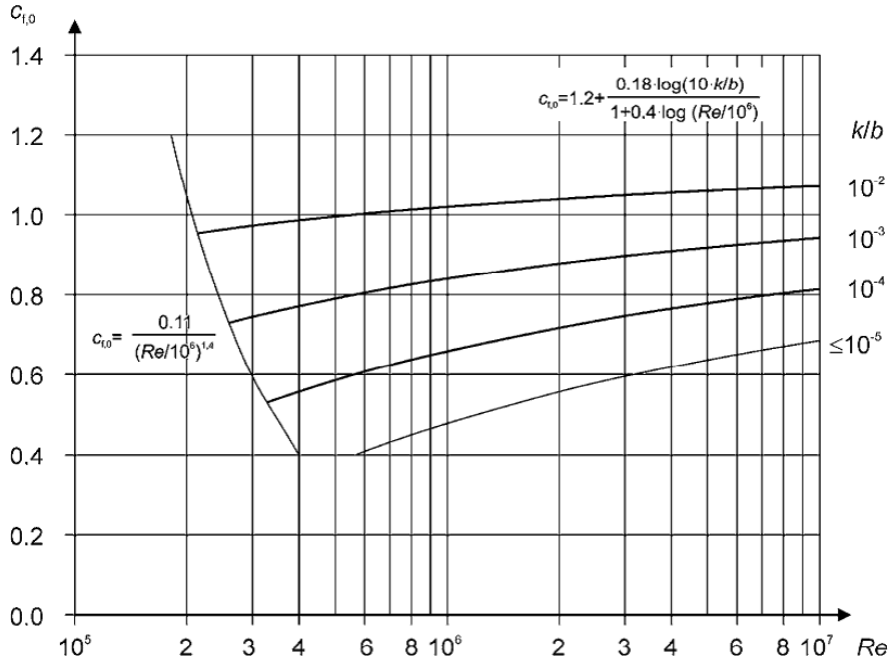

Fig. 5. Force coefficient $c_{\mathrm{f},0}$ for circular cylinder without free-end flow and for different equivalent roughness k_e/b, according to [5].

of the viscous sub-layer). It is also advisable to avoid resolving the buffer (mixing) region but also in this range of y^+ it is possible to perform reliable wind flow simulation. In the case of a wall cell being placed in the buffer region, FLUENT software blends functions between the logarithmic and laminar sub-layer values.

Figure 6 indicates that $y^+ > 135$ for $w = 33.5$ m/s and $y^+ > 50$ for $w = 11$ m/s (except for the shock and the trailing surface of the cylinder). Furthermore, it does not drop significantly below 50 for $w = 33.5$ m/s and 6 for $w = 11$ m/s. Therefore, it can be concluded that the near-wall mesh resolution is acceptable.

Following the adoption of all previous rules the problem is converged. Residuals are decreased by three orders of magnitude. The net mass imbalance is less than 0.2% of the net flux through the domain. It means that when using present models, the reliable results are obtained.

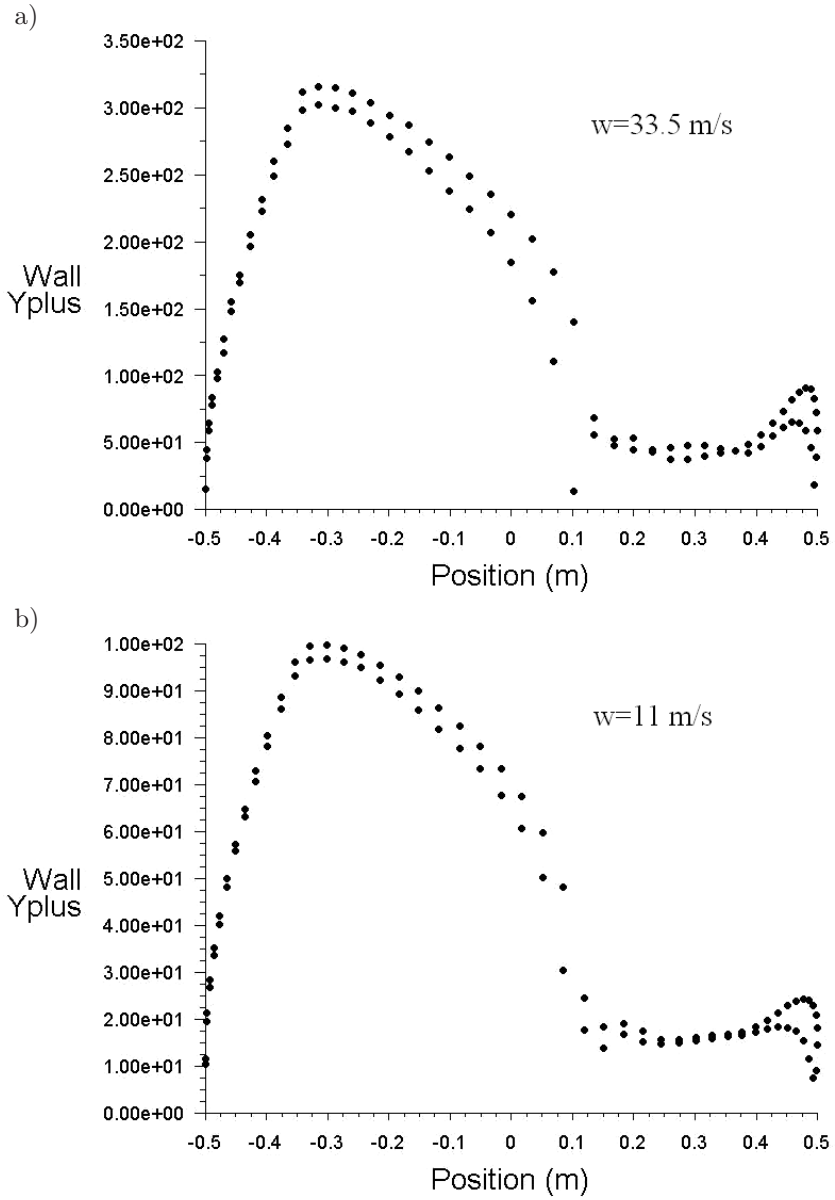

Fig. 6. y^+ distribution on the wall for: a) $w = 33.5$ m/s, b) $w = 11$ m/s.

3. Numerical model of wind flow around a part of a water slide

Dimensions, boundary conditions and the FVM grid of an exemplary numerical model of wind flow around a half of a torus are shown in Figs. 7a–c. Two types (steps) of numerical analyses are taken into account. In the first step of calculation the FLUENT software is applied to wind flow modeling. Interaction between fluid and torus is analyzed in the Static Structural software.

Boundary layer is discretized in an analogous manner to the case of calculations of wind flow around a cylinder. The volume mesh is made up of about 284 000 hexahedral cells.

Several initial calculations were performed to check sensitivity of that kind of analyses. First, the basis numerical domain and the double-wide one were compared. For the double-wide model the components P_x and P_z of the total wind force are reduced respectively by about 6% and about 3%, while the double-density grid covering the wall of the object resulted in an increase in total drag force by 3% and no change in the force component P_z.

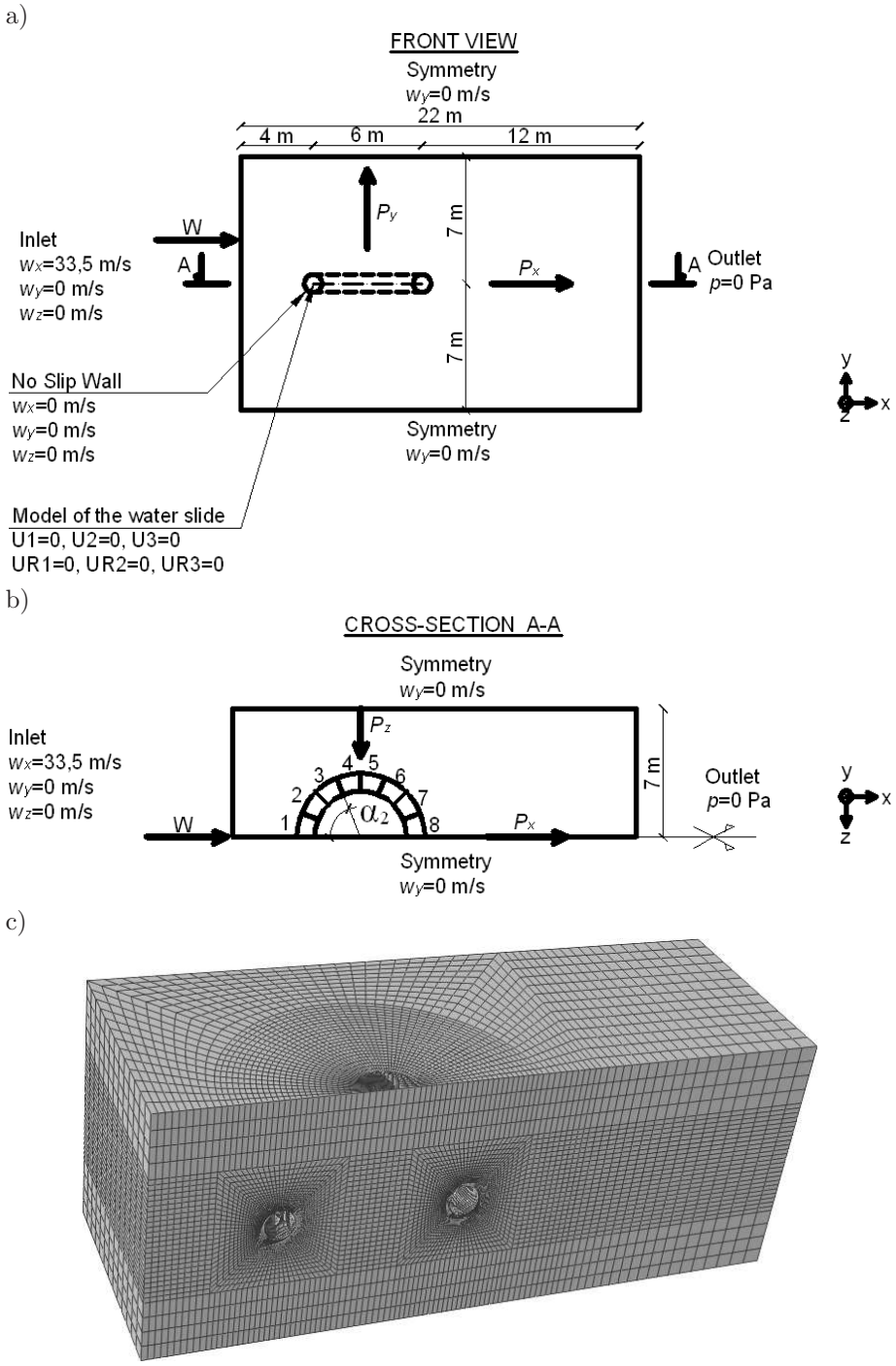

Fig. 7. Numerical model of wind flow around a part of a water slide – a half of a torus – dimensions, boundary conditions, directions of aerodynamic forces, discretization: a) front view, b) cross-section A-A, c) FVM mesh.

In order to verify if it is possible to test wind force of the entire torus with only a half of the model (symmetry boundary condition) the entire torus was also analyzed (see Figs. 8a–c). It was subjected to a wind speed $w = 33.5$ m/s. The total force P_x acting on the torus is smaller only by about 1.5% of twice the total force acting on the half-torus. The total force P_z finally equals zero. The abnormality was observed in eighth part and its mirror image of the entire torus model. Because of the randomness and turbulence in this area the difference in forces P_x in those regions reaches 11.8% and in P_z – even 13.2% while at the remaining parts from 0% to 5%. The final total value of the aerodynamic forces acting on a half or the whole torus, however, remains consistent.

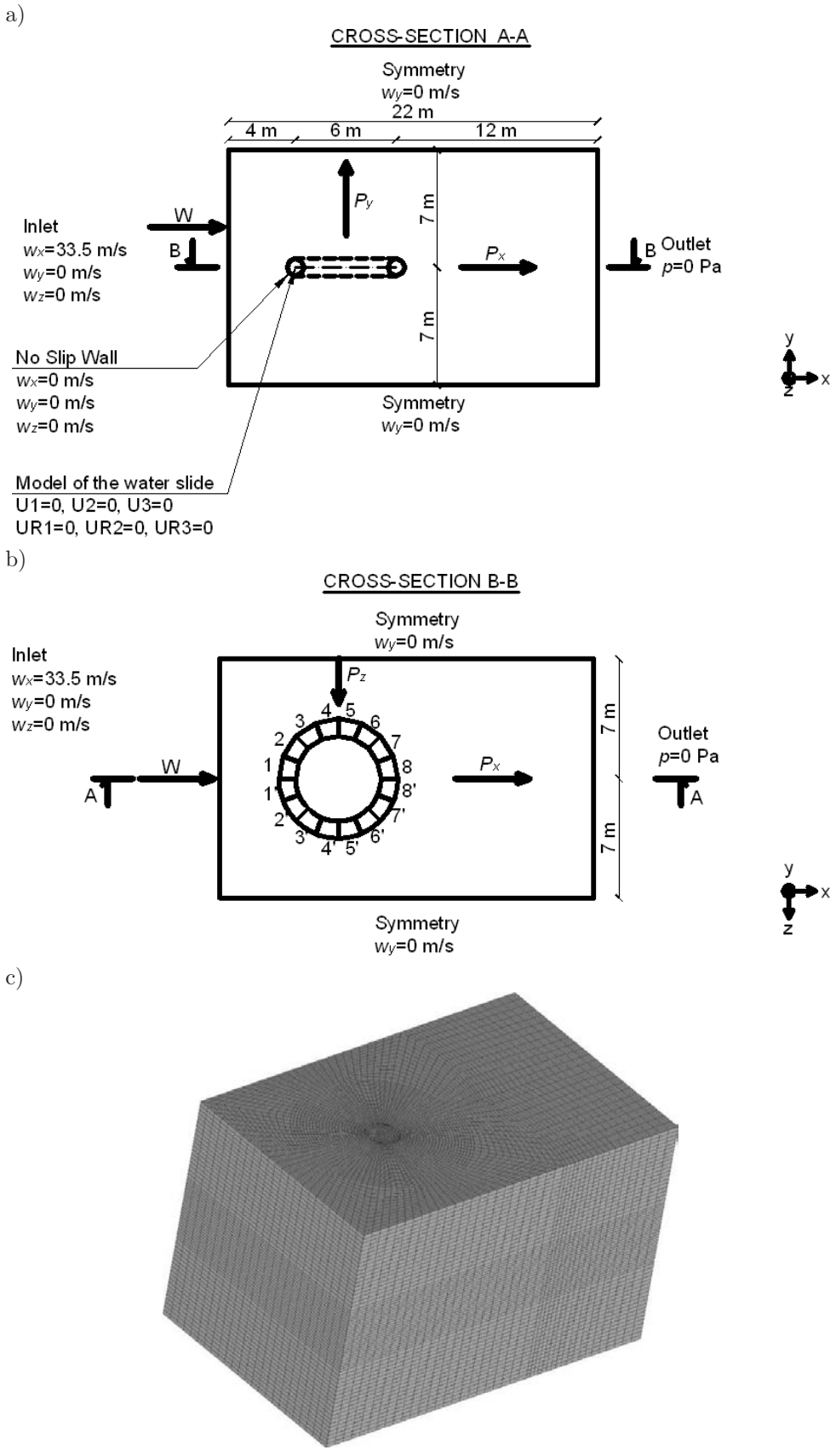

Fig. 8. Numerical model of wind flow around a part of a water slide – an entire torus – dimensions, boundary conditions, directions of aerodynamic forces, discretization: a) cross-section A-A, b) cross-section B-B, c) FVM mesh.

4. Wind actions on a part of a water slide

Analysis concerns spatial models of a part of a water slide in the shape of a half torus whose radius $R = 3.0$ m and the diameter of the track section $b = 1.0$ m, arranged horizontally (Fig. 7). Wind force of different wind speed acts on the object. The pipe is divided into eight parts that feature surface bodies (Fig. 7b). Fluid flow interacts with a solid structure. One-way force transfer (fluid $\rightarrow$ structure) is appropriate when displacements calculated in the mechanical application are not large enough to have a significant impact on the fluid analysis. In the current work the CFD analysis results (forces due to shear stress and normal pressure) at the fluid-structure interface are transferred to the mechanical model at the time step when they reach average values, and applied as loads on corresponding faces. According to [3], the results at a fluid-structure interface from a CFD analysis are used as face forces (calculated from the vector sum of the normal pressures and shear stresses) on corresponding faces in the mechanical application. The import process involves interpolating a CFD solution onto the mechanical application face mesh. Mechanical nodal values are calculated by linear interpolation from the surrounding CFD nodes. If interpolation process cannot find a face to map, then closest point is chosen. Forces can be calculated by integrating the pressure over the surface of the object.

There are two methods available for performing a one-way FSI analysis: 1) by importing loads or 2) by system coupling. Since in this paper deformations and displacements are ignored, the first method was used for its lower computational requirements.

All of this requires that the following conditions are met:

- for surface bodies the layers of thickness of 0.01 m are determined. Despite this, according to [3], by default, the shell section mid-surface is aligned with the surface body;
- it is assumed that the object does not deform under the influence of wind thus the stiffness behavior of surface bodies is declared to be rigid. In the solver rigid parts are represented by a single point that carries the inertial properties together with a discretized exterior surface that represents the geometry;
- multiple remote points work in tandem with the *remote displacement* boundary conditions. Fixed displacement constraining all degrees of freedom is applied to each part. Bodies/surfaces are in *bonded contact* thus no sliding or separation between faces or edges is allowed. It is a linear problem so only one iteration is required;
- Fig. 9 shows the division of the object surface into finite elements. The whole finite element mesh consists of 12 076 shell elements. The shell element SHELL181 is used here. It is a four-node element with six degrees of freedom at each node (three- way displacement and three angles of rotation);

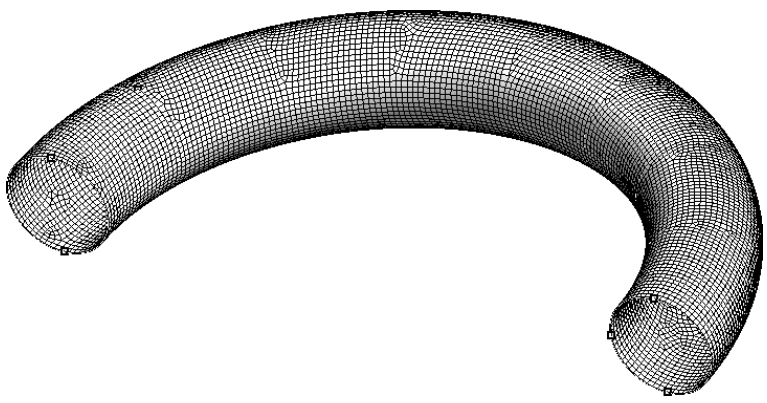

Fig. 9. FEM mesh of the numerical model of a part of a water slide.

- according to [3] shell elements assume that the nodes are at the mid-plane of the true geometry. Then forces from the *fluid-solid interface* are applied at the mid-plane by default. By using a value of 0 of the *shell thickness factor* the physical thickness and offset of the surface body nodes are ignored;
- the fluid-structure interface is a defined boundary in CFD;
- the location of the CFD boundary (with respect to the global Cartesian coordinate system) is the same as the corresponding faces in the mechanical application model;
- according to [3] and [15], an interface mesh of a fluid and a solid does not need to match but reasonably matching and fine mesh was used on curved surfaces to avoid errors in the force transfer. Similar mesh length scales maintain the load transfer resolution. Difference in element's normal directions across interface could produce twisting on coarse meshes with surface curvature – force vector is transferred to the solid, but does not act normal on the solid elements. If the target side of the interface is significantly coarser than the source side, then only the large scale features of the source data's profile will be captured in the data transfer. Similarly, if the target side of the interface is significantly finer than the source side, then the resulting target data will be a linearly interpolated representation of the data on the source side;
- *mapped face meshing* is used to generate structured meshes on surfaces.

In the analyses presented here 100 % of the mechanical application nodes was mapped successfully what is reported in the diagnostics.

5. Selected results of numerical calculations

In Fig. 10 the calculated drag coefficients of cylinders perpendicular to direction of wind flow using a fine mesh at different *Re* numbers are compared to the force coefficients given from the Eurocode EN 1991-1-4 (which are similar to the results determined by using a coarse mesh – see the upper curve). Following the adoption of more restrictive rules of discretization, the drag coefficients proved to be smaller by about 30% and they are consistent with the results measured in the cryogenic wind tunnel and described in [1]. Furthermore, a very good agreement is observed between results of the mean pressure distribution on the cylinder surface at $Re = 2.2 \times 10^6$ in this paper (Fig. 11) and two sets of experimental data described in [17] and [19] and also numerical results in [4]. A good agreement is observed between results of the mean pressure distribution on the cylinder surface in this paper and an experimental data described in [14] and European code [5].

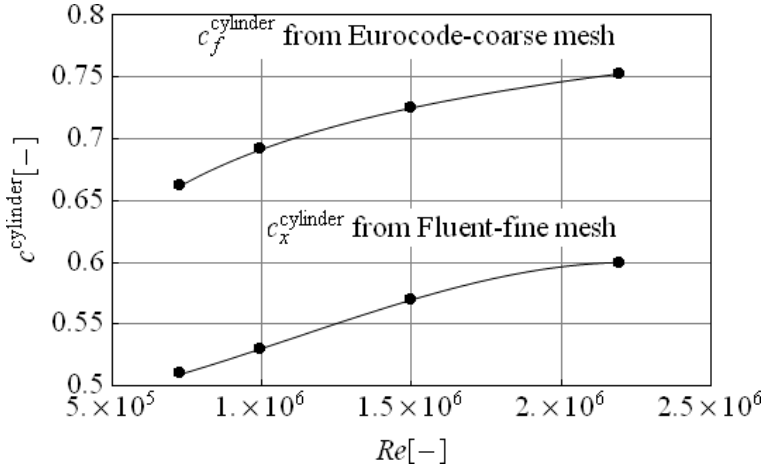

Fig. 10. Variations of drag and force coefficient with the Reynolds-number according to the value of equivalent surface roughness of $k_e = 0.15$ mm.

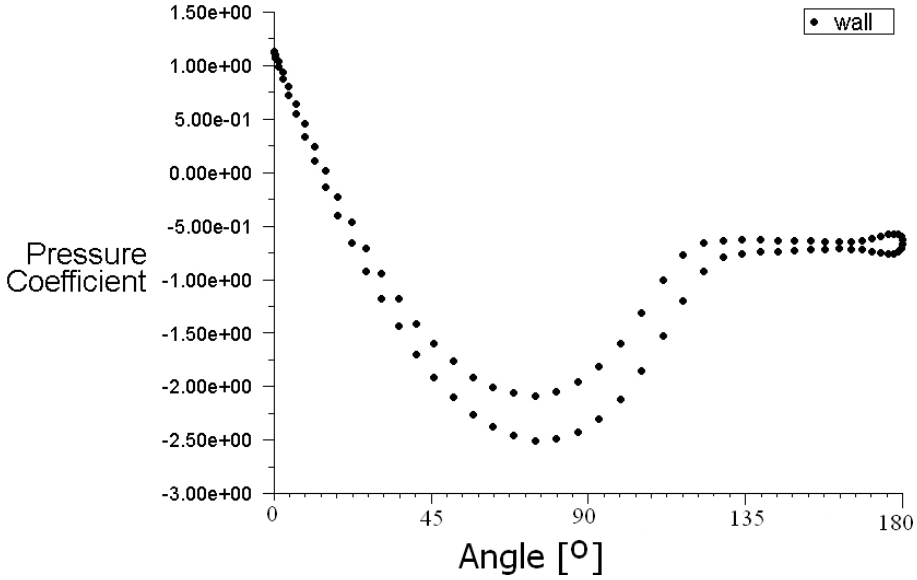

Fig. 11. Wind pressure coefficient C_p distribution on a wall at $Re = 2.2 \times 10^6$.

The reaction forces at different parts of the torus were determined using ANSYS Static Structural and were calculated as the sum of the reaction forces at the parts cut by angle α_2 (in Fig. 7b this angle comprises three parts). As a part of the verification calculations analysis was performed by dividing the half-torus into four parts. The results remained unchanged.

Figure 12 presents the pressure distribution around the near-wall region of the model and Fig. 13 presents streamlines in this region. Both of them show that in the case of a torus in horizontal position a path of disturbed flow is created behind a windward quarter. Vortices are formed almost symmetrically. The turbulent boundary layer separation point moves back. The flow after the leeward quarter of the torus is unsteady, swirling, asymmetrical, chaotic and random. The value of the drag coefficient decreases. This is the supercritical range of the *Re* number.

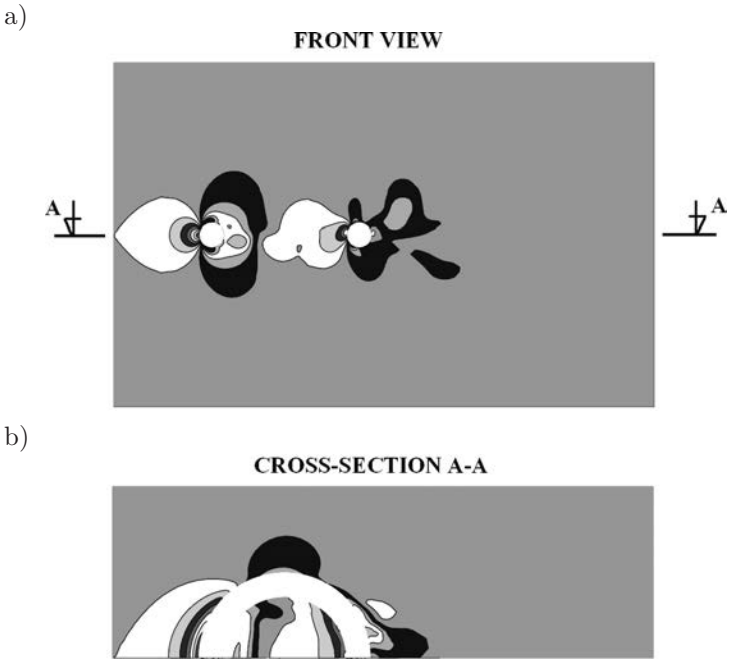

Fig. 12. Pressure distribution in the: a) front view, b) cross-sections of the model.

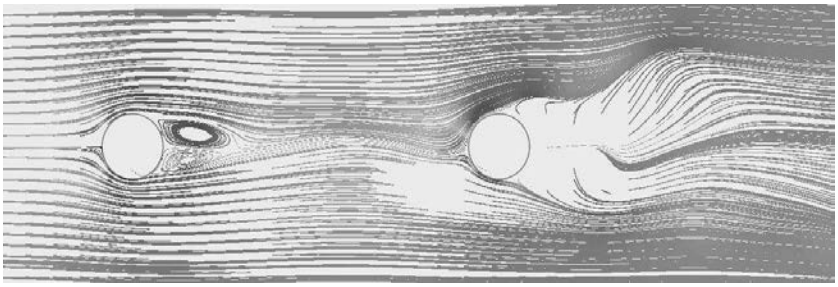

Fig. 13. Streamlines at $w = 33.5$ m/s.

Figure 14 shows variations of the aerodynamic forces with the α_2 angle and the wind flow velocity using coarse and fine meshes. The largest increase in the drag force P_x was observed on the first two and the last two parts of half of the torus arranged horizontally. The pressure force acts on the wall of parts fourth–sixth by reducing the flow velocity in front of the leeward quarter. At seventh and eighth part randomness and turbulence are observed. The value of the drag coefficient decreases.

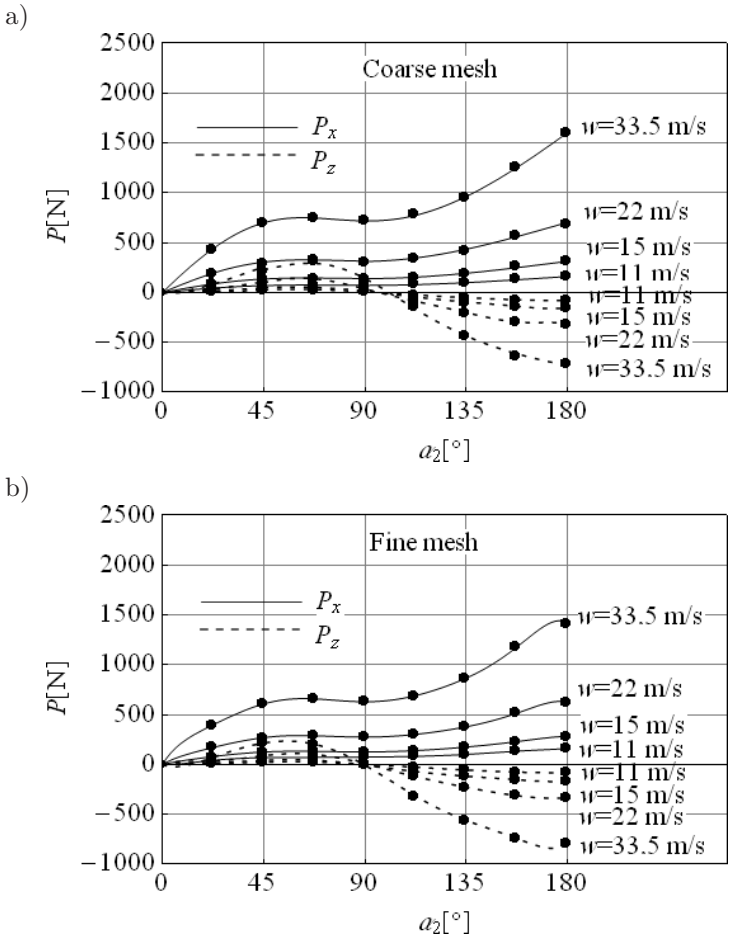

Fig. 14. Variations of the aerodynamic forces with the α_2 angle and wind flow velocity by using coarse and fine meshes.

The drag force P_x of the whole half of the torus determined by using a coarse mesh is maximally greater by about 12% than the drag force determined by using a fine mesh at the wind speed of 33.5 m/s. The P_z force is smaller by about 6%.

6. Conclusions

In this paper one-way fluid-structure interaction was used. It enabled the calculations of the wind actions on each part of the water slide in a simplified shape of half of a torus. In the partitioned approach equations governing the flow and the behavior of the structure were solved separately, with two different solvers.

Calculation of gas flow is a complicated task, requiring knowledge concerning the adoption of appropriate boundary conditions, selecting an appropriate model of turbulence and precise FEM and FVM mesh in the area around the wall of the object in order to accurately reflect the changes in the velocity gradient in the boundary layer. Good stability properties and low computational costs were achieved by using the *shear-stress transport (SST) k-ω* turbulence model. The analysis has also focused on grid refinements. Following the adoption of more restrictive rules of a discretization, the drag coefficients of the cylinders perpendicular to direction of wind flow determined by using fine mesh proved to be smaller by about 30% than the force coefficients obtained from the Eurocode EN 1991-1-4 or by using a coarse mesh, and they are consistent with the measured results in the cryogenic wind tunnel and described in [1]. While the drag force P_x of the whole half of the torus determined by using a coarse mesh is maximally greater by about 12% at the wind speed of 33.4 m/s than the drag force determined by using a fine mesh the P_z force is smaller by about 6%.

In the case of a torus in horizontal position vortices are formed almost symmetrically behind a windward quarter of the torus. The flow after the leeward quarter of the torus is unsteady, swirling, asymmetrical, chaotic and random. The value of the drag coefficient decreases. This is the supercritical range of the *Re* number.

The largest increase in the drag force P_x was observed on the first two and the last two parts of half of the torus arranged horizontally. The pressure force acts on the wall of parts fourth–sixth by reducing the flow velocity in front of the leeward quarter.

However, the numerical results are influenced by: 1) precision of numerical models dictated by the lengthy calculation, 2) adoption of the average value of the drag coefficient in a turbulent flow by the user of the program, 3) changes in the pressure distribution on the walls of the object at different time steps even for the same average value of the drag coefficient, particularly in the area exposed to actions of strong pressure force (fourth, fifth and sixth part of the torus), 4) the method and quality of approximation of the solutions of the Navier-Stokes and Reynolds equations, 5) the assumption that the dependencies $P(\alpha_2)$ change in proportion to the square of the wind speed (see, e.g., (10)).

Acknowledgement

This research was supported in part by Polish Grid Infrastructure PL-Grid project.

References

[1] T. Adachi. The effect of surface roughness of a body in the high Reynolds – number flow. *International Journal of Rotating Machinery*, **2**: 23–32, 1995.
[2] J. Anderson. *Computational Fluid Dynamics. The basics with applications*. McGraw-Hill, Inc., USA, 1995.
[3] ANSYS Documentation for Release 14.5/Customer Training Material. ANSYS Inc., 2012.
[4] P. Catalano, M. Wang, G. Iaccarino, P. Moin. Numerical simulation of the flow around a circular cylinder at high Reynolds numbers. *International Journal of Heat and Fluid Flow*, **24**: 463–469, 2003.
[5] *prEN 1991-1-4, Eurocode 1: Actions on structures – Part 1–4: General actions – Wind actions with National Annex*. CEN, Brussels 2005; PKN, Warszawa, 2008.
[6] *2D NACA 0012 Airfoil Validation Case. SST Model Results*. Langley Research Center. Turbulence Modeling Resource. Accessed http://turbmodels.larc.nasa.gov/naca0012_val_sst.html.
[7] *Introduction to Abaqus/CFD*. Dassault Systemes, 2010.
[8] K. Jeżowiecka-Kabsch, H. Szewczyk. *Fluid Mechanics* [in Polish: *Mechanika płynów*]. Oficyna Wydawnicza Politechniki Wrocławskiej. Wrocław, 2001.

[9] T. Jiyuan, H. Guan, L. Chaoqun. *Computational Fluid Dynamics. A Practical Approach*. Elsevier Inc., USA, 2008.
[10] F. Menter, T. Esch. *Elements of industrial heat transfer predictions*. COBEM 2001, 16th Brazilian Congress of Mechanical Engineering, 2001.
[11] F. Menter. Two-equation eddy-viscosity turbulence models for engineering applications. *AIAA Journal*, **32**: 1598–1605, 1994.
[12] F. Menter. Zonal two equation k-ω turbulence models for aerodynamic flows. *AIAA Paper*: 93–2906, 1993.
[13] A. Padewska. *Determination of response of nontypical shape objects on wind load. Current research and analysis of civil engineering. The scientific works of PhD students.* Collective work edited by Joanna Bzówka [in Polish: *Wyznaczanie siły oddziaływania wiatru na obiekty o nietypowym kształcie. Aktualne badania i analizy z inżynierii lądowej. Prace naukowe doktorantów*]. Gliwice, Wydaw. Politechniki Śląskiej, 621–628, 2013.
[14] A. Roshko. Experiments on the flow past a circular cylinder at very high Reynolds number. *Journal of Fluid Mechanics*, **10**: 345–356, 1961.
[15] *Solving FSI Applications Using ANSYS Mechanical and ANSYS FLUENT. Training course*. ANSYS Inc., 2012.
[16] H. Versteeg, W. Malalasekera. *An Introduction to computational fluid dynamics: the finite volume method*. Pearson Education Ltd., 2007.
[17] K. Warschauer, J. Leene. Experiments on mean and fluctuating pressures of circular cylinders at cross flow at very high Reynolds number. *Proc. Int. Conf. on Wind Effects on Buildings and Structures*, pp. 305–315. Tokyo, Japan, 1971.
[18] D. Wilcox. *Turbulence modelling for CFD*. DCW Industries, USA, 2006.
[19] M. Zdravkovich. *Flow around circular cylinders. Fundamentals*, vol. 1, chapter 6. Oxford University Press, 1997.